

# Fast Algorithms for Phase Diversity-Based Blind Deconvolution

Curtis R. Vogel<sup>a</sup>, Tony Chan<sup>b</sup> and Robert Plemmons<sup>c</sup>

<sup>a</sup> Department of Mathematical Sciences  
Montana State University  
Bozeman, MT 59717-0240 USA

<sup>b</sup> Department of Mathematics  
UCLA  
Los Angeles, CA 90095-1555 USA

<sup>c</sup> Department of Mathematics and Computer Sciences  
Wake Forest University  
Winston-Salem, NC 27109 USA

## ABSTRACT

Phase diversity is a technique for obtaining estimates of both the object and the phase, by exploiting the simultaneous collection of two (or more) short-exposure optical images, one of which has been formed by further blurring the conventional image in some known fashion. This paper concerns a fast computational algorithm based upon a regularized variant of the Gauss-Newton optimization method for phase diversity-based estimation when a Gaussian likelihood fit-to-data criterion is applied. Simulation studies are provided to demonstrate that the method is remarkably robust and numerically efficient.

**Keywords:** phase diversity, blind deconvolution, phase retrieval, quasi-Newton methods

## 1. INTRODUCTION

Phase diversity-based blind deconvolution is a technique for obtaining estimates of both the object and the phase in optical image deblurring. It involves the simultaneous collection of two (or more) short-exposure images. One of these is the object that has been blurred by unknown aberrations and the other is collected in a separate channel by blurring the first image by a known amount, e.g., using a beam splitter and an out-of-focus lens. Using these two images as data, one can set up a mathematical optimization problem (typically using a maximum likelihood formulation) for recovering the object as well as the phase aberration. The mathematics of this recovery process was first described by Gonsalves.<sup>1</sup> Later, Paxman et al<sup>2</sup> extended Gonsalves' results, allowing for more than two diversity measurements and for non-Gaussian likelihood functions. The work presented here aims at improving the numerical efficiency of the restoration procedure when a Gaussian likelihood, or least squares, fit-to-data criterion is used. A variant of the Gauss-Newton method for nonlinear least squares<sup>3</sup> is introduced to solve the optimization problem. Unlike first order (gradient-based) methods previously employed,<sup>2</sup> this scheme makes direct use of second order (Hessian) information, thereby achieving much more rapid convergence rates. When combined with appropriate stabilization, or regularization, the method is remarkably robust, providing convergence even for poor initial guesses without the aid of a globalization technique, e.g., a line search, to guarantee convergence.

This paper is organized as follows. Section 2 begins with a mathematical description of image formation in the context of phase diversity. We assume spatial translation invariance, and we assume that light emanating from the object is incoherent.<sup>4</sup> Discussion of the mathematical model for phase diversity-based blind deconvolution is followed by the formulation of a mathematical optimization problem whose solution yields both the unknown phase

---

Other author information: (Send correspondence to Curtis R. Vogel)

Curtis R. Vogel: e-mail: vogelmath.montana.edu; world wide web url://www.math.montana.edu/~vogel

Tony Chan: e-mail: chan@math.ucla.edu; world wide web url://www.math.ucla.edu/~chan

Robert Plemmons: e-mail: plemmons@mthsc.wfu.edu; world wide web url://www.mthsc.wfu.edu/~plemmons

aberration and the unknown object. The cost functional to be minimized is of *regularized least squares* type, taking the form

$$J[\phi, f] = J_{data}[\phi, f] + \frac{\gamma}{2} \|f\|^2 + \alpha J_{reg}[\phi]. \quad (1)$$

Here  $\phi$  and  $f$  represent the phase and the object, respectively, and  $\gamma$  and  $\alpha$  are positive parameters which quantify the trade-off between goodness of fit to the data and stability. The first term on the right hand side of (1) is a least squares fit-to-data term; the second term provides stability with respect to perturbations in the object; and the third term provides stability with respect to perturbations in the phase. Stabilization provides several advantages: It dampens spurious oscillations in the phase and the object; and it helps “convexify” the optimization problem, getting rid of spurious small-scale minima of the cost functional. A solution can then be computed in a fast, robust manner using local optimization techniques like Newton’s method.

We select an object stabilization term  $\|f\|^2/2$  which is quadratic. This, combined with the fact that the fit-to-data term is quadratic in the object, allows us to formulate a reduced cost functional<sup>1,2</sup> whose only unknown is the phase  $\phi$ . We select a parameterization of the phase which is based on prior knowledge of its statistics. This parameterization leads to a natural choice of the phase regularization functional  $J_{reg}[\phi]$  in equation (1).

Section 3 addresses the computation of a minimizer for the reduced cost functional. We present a variant of the well-known Gauss-Newton method<sup>3</sup> for nonlinear least squares minimization. Results of a numerical simulation are presented in section 4. The mathematical model used in this simulation is based on the hardware configuration for a 3.5 meter telescope at the U.S. Air Force Starfire Optical Range (SOR) in New Mexico. See Ellerbroek et al<sup>5</sup> for details. The functional (1) is minimized using three different techniques: (i) the Gauss-Newton variant; (ii) standard Newton’s method; and (iii) a standard method known as BFGS.<sup>3</sup> A comparison shows that for moderately high solution accuracy, the first method is superior when computational effort is measured in terms of iteration count. Finally, in section 5 we present a summary and a discussion of future directions of our work.

## 2. MATHEMATICAL BACKGROUND

### 2.1. Mathematical Model

The  $k^{th}$  diversity image is given by

$$d_k = s[\phi + \theta_k] \star f + \eta_k, \quad k = 1, \dots, K, \quad (2)$$

where  $\eta_k$  represents noise in the data,  $f$  is the unknown object,  $s$  is the point spread function (PSF),  $\phi$  is the unknown phase function,  $\theta_k$  is the  $k^{th}$  phase diversity function, and  $\star$  denotes convolution product,

$$(s \star f)(\mathbf{x}) = \int \int_{\mathbb{R}^2} s(\mathbf{x} - \mathbf{y}) f(\mathbf{y}) d\mathbf{y}, \quad \mathbf{x} \in \mathbb{R}^2. \quad (3)$$

Assuming that light emanating from the object is incoherent, the dependence of the PSF on the phase is given by

$$s[\phi] = |\mathcal{F}(pe^{i\phi})|^2, \quad (4)$$

where  $p$  denotes the pupil, or aperture, function,  $i = \sqrt{-1}$ , and  $\mathcal{F}$  denotes the 2-D Fourier transform,

$$(\mathcal{F}h)(\mathbf{y}) = \int \int_{\mathbb{R}^2} h(\mathbf{x}) e^{-i2\pi \mathbf{x} \cdot \mathbf{y}} d\mathbf{x}, \quad \mathbf{y} \in \mathbb{R}^2. \quad (5)$$

The pupil function  $p = p(x_1, x_2)$  is determined by the extent of the telescope’s primary mirror.

In atmospheric optics,<sup>6</sup> the phase  $\phi(x_1, x_2)$  quantifies the deviation of the wave front from a reference planar wave front. This deviation is caused by variations in the index of refraction (wave speed) along light ray paths, and is strongly dependent on air temperature. Because of turbulence, the phase varies with time and position in space and is often modeled as a stochastic process.

Additional changes in the phase  $\phi$  can occur after the light is collected by the primary mirror, e.g., when adaptive optics are applied. This involves mechanical corrections obtained with a deformable mirror to restore  $\phi$  to planarity. By placing beam splitters in the light path and modifying the phase differently in each of the resulting paths, one

can obtain more independent data. The phase diversity functions  $\theta_k$  represent these deliberate phase modifications applied *after* light is collected by the primary mirror. Easiest to implement is *defocus blur*, modeled by a quadratic

$$\theta_k(x_1, x_2) = b_k (x_1^2 + x_2^2), \quad (6)$$

where the parameters  $b_k$  are determined by defocus lengths. In practice, the number of diversity images is often quite small, e.g.,  $K = 2$  in the numerical simulations to follow. In addition, one of the images, which we will denote using index  $k = 1$ , is obtained with no deliberate phase distortion, i.e.,  $\theta_1 = 0$  in (2).

## 2.2. Cost Functionals

To estimate phase  $\phi$  from phase diversity data (2), we minimize the regularized least squares cost functional

$$J = J[\phi, f] = \frac{1}{2} \left( \sum_{k=1}^K \int \int_{\mathbb{R}^2} [(s_k \star f)(\mathbf{x}) - d_k(\mathbf{x})]^2 d\mathbf{x} \right) + \frac{\gamma}{2} \int \int_{\mathbb{R}^2} f(\mathbf{x})^2 d\mathbf{x} + \alpha J_{reg}[\phi], \quad (7)$$

where  $s_k = s[\phi + \theta_k]$ . Here  $J_{reg}[\phi]$  is a regularization functional, whose purpose is to establish stability with respect to perturbations in  $\phi$ . Similarly, the term  $\int \int_{\mathbb{R}^2} f(\mathbf{x})^2 d\mathbf{x}$  establishes stability with respect to perturbations in  $f$ .  $\gamma$  and  $\alpha$  are positive regularization parameters, which quantify the tradeoff between goodness of fit to the data and stability.

Note that  $J$  is quadratic in the object  $f$ . This enables us to solve for  $f$  by fixing  $\phi$  and minimizing with respect to  $f$ . Let upper case letters denote Fourier transforms and hold  $\phi$  constant. Using the Convolution Theorem and the fact that the Fourier transform is norm preserving, one obtains from (7)

$$J = J[F] = \frac{1}{2} \int \int_{\mathbb{R}^2} \left[ \sum_{k=1}^K |S_k(\mathbf{y})F(\mathbf{y}) - D_k(\mathbf{y})|^2 + \gamma |F(\mathbf{y})|^2 \right] d\mathbf{y} + \text{constant}. \quad (8)$$

This has as its minimizer

$$F(\mathbf{y}) = \frac{\sum_{k=1}^K S_k^*(\mathbf{y})D_k(\mathbf{y})}{\gamma + \sum_{k=1}^K |S_k(\mathbf{y})|^2}, \quad (9)$$

where the superscript  $*$  denotes complex conjugate. The estimated object is then

$$f = \mathcal{F}^{-1}(F) = \int \int_{\mathbb{R}^2} F(\mathbf{y}) e^{i2\pi \mathbf{x} \cdot \mathbf{y}} d\mathbf{y}. \quad (10)$$

Note that when  $K = 1$ , (9)-(10) give the inverse Wiener filter estimate for the solution of the deconvolution problem  $s \star f = d$ .

Substituting (9) back into (7), we obtain the reduced cost functional

$$J = J[\phi] = \frac{1}{2} \int \int_{\mathbb{R}^2} t[\phi](\mathbf{y}) d\mathbf{y} + \alpha J_{reg}[\phi], \quad (11)$$

where, suppressing the dependence on  $\mathbf{y}$ , the integrand

$$t[\phi] = \sum_{k=1}^K |D_k|^2 - \frac{|\sum_{k=1}^K D_k^* S_k[\phi]|^2}{Q[\phi]} \quad (12)$$

$$= \frac{\sum_{k=1}^K \sum_{j=1}^{k-1} |D_k S_j[\phi] - D_j S_k[\phi]|^2 + \gamma \sum_{k=1}^K |D_k|^2}{Q[\phi]}, \quad (13)$$

with

$$Q[\phi] = \gamma + \sum_{k=1}^K |S_k[\phi]|^2. \quad (14)$$

Derivation of (12) from (7) is very similar to the derivation in Paxman et al.<sup>2</sup> See Appendix A for verification of the equality of (12) and (13).

### 2.3. Parameterization of Phase

Because of atmospheric turbulence, the phase varies with both time and position in space.<sup>6</sup> Adaptive optics systems use deformable mirrors to correct for these phase variations. Errors in this correction process arise from a variety of sources, e.g., errors in the measurement of phase, inability of mirror to conform exactly to the phase shape, and lag time between phase measurement and mirror deformation. The phase aberrations resulting from an adaptive optics system are often modeled as realizations of a stochastic process. Assuming that this process is second order stationary with zero mean, it is characterized by its covariance function,

$$A(\mathbf{x}, \mathbf{y}) = \mathcal{E}(\phi(\mathbf{x}, \cdot), \phi(\mathbf{y}, \cdot)), \quad (15)$$

where  $\mathcal{E}$  denotes the expectation (temporal ensemble averaging) operator. This is a symmetric, positive function. Under certain mild conditions on  $A$ , the the associated covariance operator

$$\mathcal{A}f(\mathbf{x}) = \int \int_{\mathbb{R}^2} A(\mathbf{x}, \mathbf{y}) f(\mathbf{y}) d\mathbf{y} \quad (16)$$

is compact and self-adjoint. Hence it has a sequence of eigenvalues  $\lambda_j$  which decay to zero and corresponding eigenvectors  $\xi_j(\mathbf{x})$  which form an orthonormal basis for  $L^2(\mathbb{R}^2)$ . This eigendecomposition can be formally expressed as

$$\mathcal{A} = \mathcal{V} \text{diag}(\lambda_j) \mathcal{V}^*,$$

where  $\mathcal{V} : \ell^2 \rightarrow L^2(\mathbb{R}^2)$  is given by

$$\mathcal{V}\mathbf{c} = \sum_{j=1}^{\infty} c_j \xi_j(\mathbf{x}), \quad \mathbf{c} = (c_1, c_2, \dots) \in \ell^2.$$

This provides a means for generating simulated phase functions having the desired covariance structure. Letting  $w$  denote a simulated white noise vector, take

$$\phi(\mathbf{x}) = \mathcal{A}^{1/2}w = \mathcal{V} \text{diag}(\lambda_j^{1/2}) \mathcal{V}^*w = \sum_j \lambda_j^{1/2} \langle w, \xi_j \rangle \xi_j(\mathbf{x}), \quad (17)$$

where pointed brackets denote the complex inner product on  $L^2(\mathbb{R}^2)$ ,

$$\langle g, h \rangle = \int \int_{\mathbb{R}^2} g(\mathbf{x}) h^*(\mathbf{x}) d\mathbf{x}. \quad (18)$$

This also provides a natural regularization, or stabilization, functional

$$J_{reg}[\phi] = \frac{1}{2} \langle \mathcal{A}^{-1}\phi, \phi \rangle = \frac{1}{2} \sum_j \frac{|c_j|^2}{\lambda_j}, \quad (19)$$

where the  $c_j$ 's are the coefficients in the eigenvector expansion of  $\phi$ ,

$$\phi(\mathbf{x}) = \sum_{j=1}^m c_j \xi_j(\mathbf{x}). \quad (20)$$

## 3. NUMERICAL OPTIMIZATION

### 3.1. Gradient and Hessian Computations

Newton's method for the minimization of (11) takes the form of the iteration

$$\phi^{k+1} = \phi^k - H[\phi^k]^{-1}g[\phi^k], \quad k = 0, 1, \dots, \quad (21)$$

where  $g[\phi]$  is the gradient of  $J = J[\phi]$ ,  $H[\phi]$  denotes the Hessian, and  $\phi^0$  is an initial guess. In Appendix B, we derive from (11)-(12) the following expression for the gradient of  $J$ ,

$$g[\phi] = -2 \sum_{k=1}^K \text{Imag}(H_k^*[\phi] \mathcal{F}(\text{Real}(h_k[\phi] \mathcal{F}^{-1}V_k[\phi]))) + \alpha \mathcal{A}^{-1}\phi, \quad (22)$$

where  $\mathcal{A}$  is the covariance operator for the phase, cf., (16),  $\text{Real}(z)$  and  $\text{Imag}(z)$  denote real and imaginary parts of a complex number  $z$ , respectively, and

$$H_k[\phi] = pe^{i(\phi+\theta_k)}, \quad h_k[\phi] = \mathcal{F}^{-1}(H_k[\phi]), \quad (23)$$

$$s_k[\phi] = |h_k[\phi]|^2, \quad S_k[\phi] = \mathcal{F}(s_k[\phi]), \quad (24)$$

$$V_k[\phi] = F^*[\phi]D_k - |F[\phi]|^2 S_k[\phi], \quad (25)$$

with  $F[\phi]$  the Fourier transform of the estimated object given in (9) and  $D_k$  the Fourier transform of the data. With the exception of the  $\text{Real}(\cdot)$  in equation (22), when  $\gamma = 0$ , this reduces to formula (22)-(23) in Paxman et al.<sup>2</sup>

If the phase is represented by a linear combination (20), then by the chain rule the corresponding discrete gradient is a vector in  $\mathbb{R}^m$  with entries

$$[\mathbf{g}]_j = \langle g, \xi_j \rangle, \quad j = 1, \dots, m,$$

and the (discrete) Hessian is an  $m \times m$  matrix with  $ij^{\text{th}}$  entry

$$\mathbf{H}_{ij} = \langle H[\phi]\xi_j, \xi_i \rangle, \quad 1 \leq i, j \leq m. \quad (26)$$

The Hessian entries can be approximately computed from (26) using finite differences of the gradient, e.g.,

$$H[\phi]\xi_j \approx \frac{g[\phi + \tau\xi_j] - g[\phi]}{\tau}$$

for  $\tau$  relatively small. When combined with iteration (21), this approach is known as the finite difference Newton's method.<sup>3</sup> When  $m$  is large, this approach is not practical. A commonly used alternative is the BFGS method.<sup>3</sup> Requiring only values of the gradient, BFGS simultaneously constructs a sequence of approximate minimizers  $\phi^k$  and a sequence of symmetric positive definite (SPD) approximations to the Hessian or its inverse. While this method can be rigorously proven to be asymptotically superlinearly convergent, practical experience has shown its performance to be disappointing for highly ill-conditioned problems<sup>3</sup> like the one considered here.

Due to its robustness and good convergence properties, the method of choice for general nonlinear least squares problems is Levenberg-Marquardt.<sup>3</sup> Levenberg-Marquardt consists of a Gauss-Newton approximation to the least squares Hessian, combined with a trust region globalization scheme. The key idea is that the integral of the first term in (13) can be written as a sum of functionals of "least squares" form

$$\frac{1}{2} \|r[\phi]\|^2 = \frac{1}{2} \langle r[\phi], r[\phi] \rangle.$$

The Gauss-Newton approximation  $H_{GN}$  to the corresponding least squares Hessian is characterized by

$$\langle H_{GN}[\phi]\xi, \psi \rangle = \langle r'[\phi]\xi, r'[\phi]\psi \rangle,$$

where prime denotes differentiation with respect to  $\phi$ .  $H_{GN}$  is clearly symmetric and positive semidefinite. With the addition contribution  $\alpha\mathcal{A}^{-1}$  obtained by twice differentiating the regularization term in (19), one obtains an approximation  $H_{GN} + \alpha\mathcal{A}^{-1}$  which is SPD. Even when the true (not necessarily SPD) Hessian is available, an SPD approximation like this may be preferable. While the approximation will result in slower convergence near the exact minimizer, it is likely to be more robust in the sense that it yields convergent iterates for a much wider range of initial guesses.

In Appendix C, we derive a variant of the Gauss-Newton approximation which is based on (13). We do not derive an explicit formula for the matrix  $H_{GN}[\phi]$ . Instead, we compute the action of this matrix on a given direction vector  $\xi \in L^2(\mathbb{R}^2)$  as follows: First, for  $k = 1, \dots, K$  and  $j = 1, \dots, k-1$ , compute

$$\tilde{U}_{jk} = \tilde{D}_j \mathcal{F}(\text{Imag}[h_k^* \mathcal{F}^{-1}(H_k \xi)]) - \tilde{D}_k \mathcal{F}(\text{Imag}[h_j^* \mathcal{F}^{-1}(H_j \xi)]), \quad (27)$$

and then take

$$H_{GN}[\phi]\xi = 4 \sum_{k=1}^K \sum_{j=1}^{k-1} \text{Imag}[H_j^* \mathcal{F}(h_j \mathcal{F}^{-1}(\tilde{D}_k^* \tilde{U}_{jk})) - H_k^* \mathcal{F}(h_k \mathcal{F}^{-1}(\tilde{D}_j^* \tilde{U}_{jk}))] + \alpha\mathcal{A}^{-1}\xi. \quad (28)$$

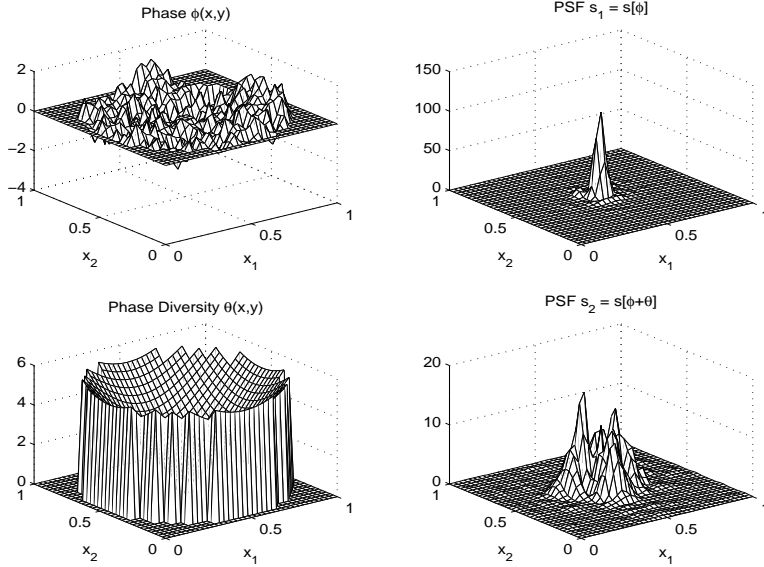


**Figure 1.** Phase, phase diversity, and corresponding PSF's.

Given a phase representation (20), one can in principle compute an  $m \times m$  Gauss-Newton-like matrix  $\mathbf{H}_{GN}$  in a manner analogous to (26). Adding the contribution from the regularization (19), one obtains the (approximate) Hessian matrix

$$\mathbf{H} = \mathbf{H}_{GN} + \alpha \mathbf{A}^{-1},$$

where now  $\mathbf{A} = \text{diag}(\lambda_1, \dots, \lambda_m)$ . If  $m$  is relatively small,  $\mathbf{H}$  can be computed explicitly and inverted. If  $m$  is large, linear systems  $\mathbf{H}\Delta\mathbf{c} = -\mathbf{g}$  can be solved using conjugate gradient (CG) iteration. The cost of each CG iteration is dominated by one Hessian matrix-vector multiplication,  $\mathbf{H}\mathbf{v}$ , per iteration, which is implemented using (27)-(28).

#### 4. NUMERICAL SIMULATION AND PERFORMANCE

The first step in the simulation process is to generate a phase function  $\phi(x_1, x_2)$ , a phase diversity function  $\theta(x_1, x_2)$ , and a pupil, or aperture, function  $p(x_1, x_2)$ . These are used to compute PSF's via equations (23)-(24). Corresponding to a telescope with a large circular primary mirror with a small circular secondary mirror at its center, the pupil function is taken to be the indicator function for an annulus. The computational domain is taken to be a  $72 \times 72$  pixel array.  $n = 888$  of these pixels lie in the support of the pupil function, which is the white region in the upper right subplot in Fig. 2. Values of the phase function  $\phi$  at these  $n$  pixels are generated from an  $n \times n$  covariance matrix in a manner analogous to (17), i.e., the phase is the product of a square root of a covariance matrix and a computer-generated discrete white noise vector. We use a covariance matrix which models phase aberrations from an adaptive optics system for a 3.5 meter telescope at the SOR. The phase used in the simulation appears in the upper left subplot in Fig. 1. The PSF  $s_1 = s[\phi]$  corresponding to this phase is shown in the upper right subplot. The quadratic phase diversity function  $\theta$  appears in the lower left subplot. To its right is the PSF  $s_2 = s[\phi + \theta]$  corresponding to the perturbed phase. In the notation of Section 2,  $\theta = \theta_2$ , while  $\theta_1$  is identically zero.

The next stage in the simulation process is to generate an object function  $f(x_1, x_2)$ , convolve it with the two PSF's, and add noise to the resulting pair of images, cf., equation (2). The convolution integrals are approximated using 2-D FFT's, and the simulated noise vectors,  $\eta_k, k = 1, 2$ , are taken from a Gaussian distribution with mean zero and variances  $\sigma_k^2$  equal to the 5 percent of the signal strengths in each image, i.e.,  $\sigma_k = .05 \times \|s_k \star f\|$ . The object is a simulated binary star, shown at the upper left in Fig. 2. The lower left subplot shows the blurred noisy image corresponding to phase  $\phi$ , while the image at the lower right corresponds to the perturbed phase  $\phi + \theta$ .

Given data consisting of the images  $d_1$  and  $d_2$  and the pupil function  $p(x_1, x_2)$  shown in Fig. 2 together with the diversity function  $\theta(x_1, x_2)$  shown in Fig. 1, the minimization problem described previously is solved numerically. The regularization parameters are chosen to be  $\gamma = 10^{-7}$  and  $\alpha = 10^{-5}$ , and the dominant  $m = 40$  eigenvectors are selected as the  $\xi_j(x_1, x_2)$ 's in the representation (20) for the phase. The reconstructed phase and object are

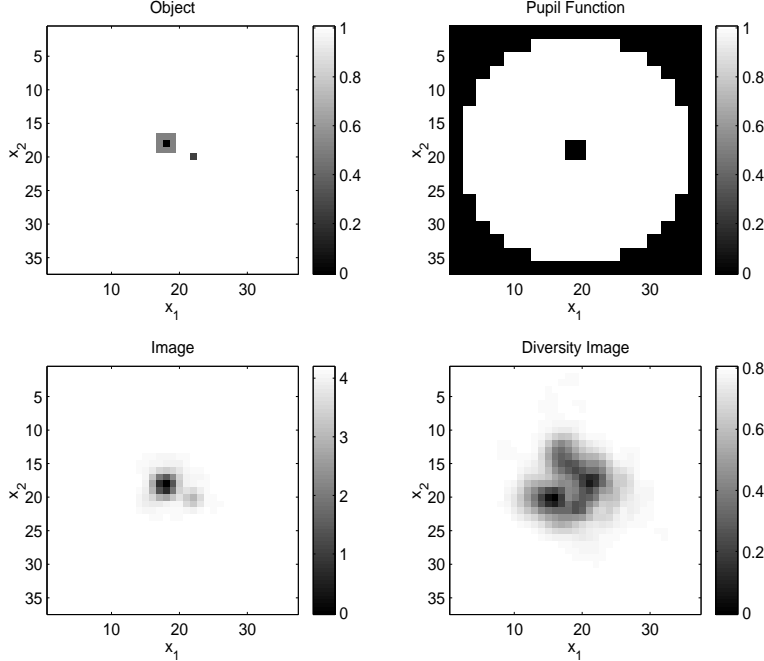


**Figure 2.** Negative grayscale plot of simulated object  $f(x_1, x_2)$  at upper left; image  $d_1 = s[\phi] \star f + \eta_1$  at lower left; and diversity image  $d_2 = s[\phi + \theta] \star f + \eta_2$  at lower right. At the upper right is a grayscale plot of the pupil, or aperture, function.

shown in Fig. 3. The parameters  $\alpha$ ,  $\gamma$ , and  $m$  were selected by trial and error to provide the best reconstructions from the given (noisy, discrete) data. If  $\alpha$  and  $\gamma$  are decreased significantly, the reconstructions degrade because of amplification of error. On the other hand, increasing these parameters significantly results in overly smoothed reconstructions. Decreasing  $m$  significantly will result in loss of resolution. Increasing  $m$  will have no effect on the reconstructions, but it will increase the computational cost due to increased size of the (discrete) Hessians.

It should be noted in Fig. 3 that the reconstructed phase is compared not against the exact phase (shown at the upper left in Fig. 1), but against the  $L^2$  projection of the exact phase onto the span of the dominant  $m$  eigenfunctions of the covariance matrix. This can be interpreted as a projection onto a “low frequency” subspace. A visual comparison of the upper left and lower left subplots in Fig. 3 shows very good agreement; the norm of the difference of the two functions being plotted differ by about 10 percent. Similarly, the reconstructed object is compared against a diffraction limited version of the true object.

Numerical performance is summarized in Figs. 4. The Gauss-Newton (GN) method, the finite difference Newton’s (FDN) method, and the BFGS method were each applied with initial guess  $\phi^0 = 0$  and same parameter values,  $\gamma = 10^{-7}$ ,  $\alpha = 10^{-5}$ , and  $m = 40$ . The latter two methods required a line search in order to converge, but GN did not. The linear convergence rate of GN and the quadratic rate for FDN can clearly be seen. While FDN and BFGS have asymptotically better convergence properties, GN required only 5 iterations to achieve phase reconstructions visually indistinguishable from the reconstructions at much later iterations. FDN required 15 iterations to achieve comparable accuracy, while BFGS required about 35 iterations. Additional overhead is incurred by these two methods in the line search implementation. In terms of total computational cost (measured by total number of FFT’s, for example), BFGS is the most efficient of the three methods due to its low cost per iteration. On the other hand, BFGS is an inherently sequential algorithm, while GN and FDN have obvious parallel implementations. Given efficient parallel implementations, clock time should be proportional to the iteration count rather than the number of FFT’s.

We also tested our algorithms on the simulated satellite image data considered by Tyler et al.<sup>7</sup> Numerical performance is summarized in Fig. 5. Somewhat different regularization parameters were used in this case ( $\alpha = 10^{-4}$  and  $\gamma = 10^{-1}$ ), while  $m = 40$  and the 5 percent noise level remains the same as in the binary star test problem. A comparison of Fig. 4 and Fig. 5 reveals the BFGS convergence history to be much the same. In the case of FDN,

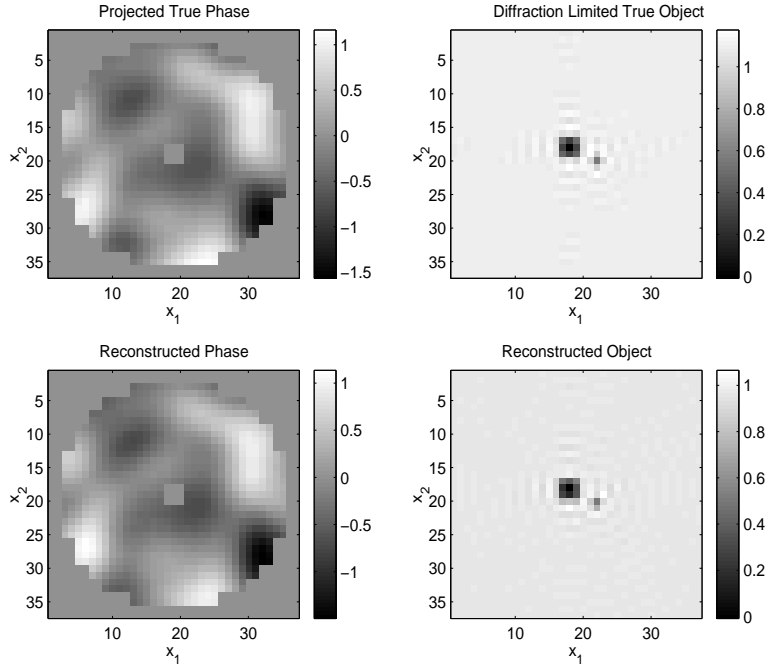


**Figure 3.** True and reconstructed phases and objects.

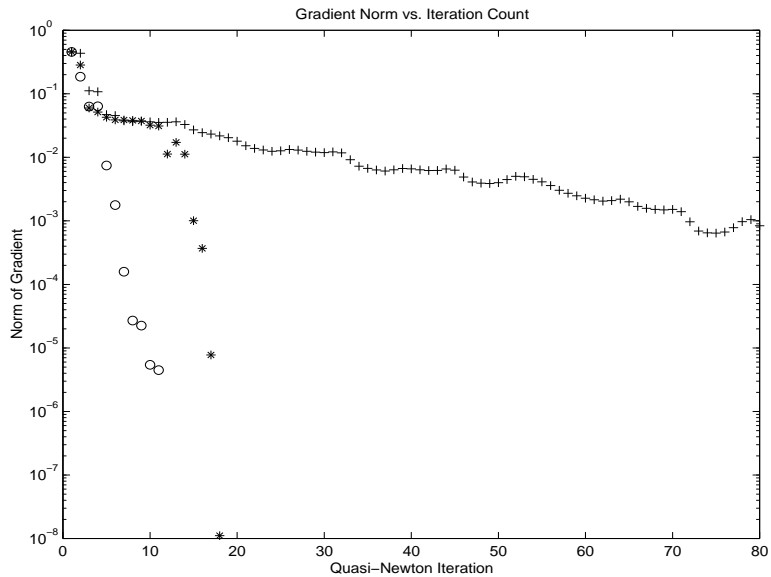


**Figure 4.** Performance of various methods for the binary star test problem, as measured by the norm of the gradient vs. iteration count. Circles (o) indicate the Gauss-Newton method; stars (\*) indicate finite difference Newton's method; and pluses (+) indicate the BFGS method.

rapid (quadratic) convergence occurs much earlier (at 8 or 9 iterations vs. at 18 or 19 iterations) for the satellite problem than for the binary star problem. As with the binary star test problem, due to the need to perform several line searches during the first few iterations, the actual cost of FDN is somewhat higher than what the 8 or 9 iterations might indicate.

For GN, we obtained rapid decrease in the norm of the gradient for the first 3 or 4 iterations with both test problems. This rapid decrease continues for later iterations in the binary star case. For the satellite test problem on the other hand, the GN convergence rate slows considerably at later iterations. However, after 3 iterations there

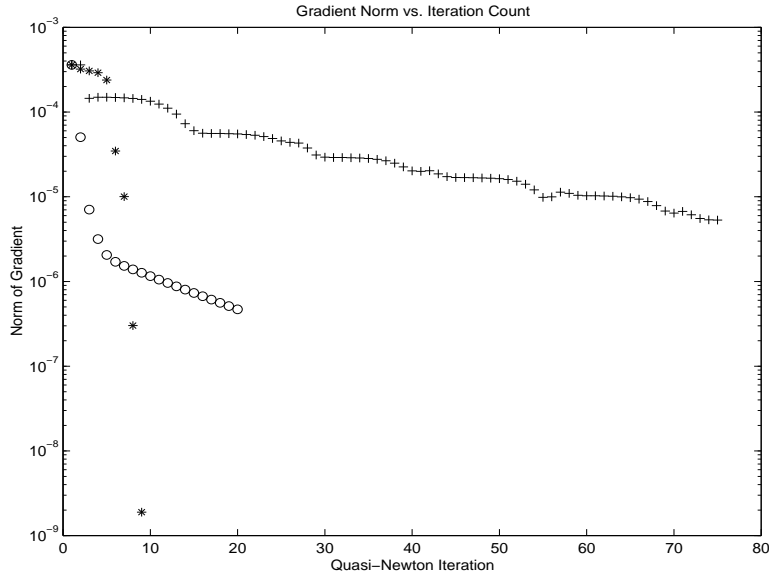


**Figure 5.** Performance of various methods for the satellite test problem, as measured by the norm of the gradient vs. iteration count. Circles (o) indicate the Gauss-Newton method; stars (\*) indicate finite difference Newton’s method; and pluses (+) indicate the BFGS method.

is almost no change in the reconstructed phase and object. Hence, to obtain “reasonably accurate” reconstructions with GN, no more than 4 iterations are necessary for the satellite test problem. As in the previous test problem, GN required no line searches.

## 5. DISCUSSION

This paper has presented a fast computational algorithm for simultaneous phase retrieval and object recovery in optical imaging. The approach uses phase diversity-based phase estimation with a maximum likelihood fit-to-data criterion when a Gaussian noise model is applied with appropriate stabilization of the cost functional (1). Three methods, full Newton, Gauss-Newton, and BFGS, for minimizing the resulting least squares cost functional were compared in numerical simulations. The Newton and Gauss-Newton make use of both first order (gradient) and second order (Hessian) information. Their implementations for our two test problems are highly parallelizable, in comparison to the BFGS secant updating method. The full Newton approach required a good initial guess, while Gauss-Newton is robust, even with a poor initial guess and without globalization, i.e., a line search. In particular, simulation studies indicate that the method is remarkably robust and numerically efficient for our problem.

Improvements and extensions of this work being considered include following projects.

- Parallel implementation. The code, currently in MATLAB, is being converted to C for implementation on the massively parallel IBM SP2 at the Air Force Maui High Performance Computing Center. This project is partially in conjunction with the AMOS/MHPCC R&D Consortium Satellite Image Reconstruction Study.<sup>7</sup> The gradient of our reduced cost functional as well as the Gauss-Newton Hessian-vector products can be efficiently evaluated in parallel. Our objective is to achieve a parallel implementation where the run-time is essentially independent of the phase parameterization value  $m$  discussed in §3.1.
- Phase-diversity based phase retrieval. The recovery of phase aberrations induced by atmospheric turbulence using phase diversity methods has recently been compared to classical Shack-Hartman wavefront sensing.<sup>8</sup> Here, the object itself is assumed known, e.g., a point source from a natural or laser guide star. The wavefront phase aberrations estimates are used to drive a closed loop adaptive optics system for real-time control of deformable mirrors used in optical image reconstruction. Speed is of course essential in these phase retrieval computations, and we plan to consider this application in our future work.

## APPENDIX A. DERIVATION OF EQUATION (13)

$$\begin{aligned}
\sum_{k=1}^K \sum_{j=1}^{k-1} |D_k S_j - D_j S_k|^2 &= \frac{1}{2} \sum_{k=1}^K \sum_{j=1}^K |D_k S_j - D_j S_k|^2 \\
&= \sum_{k=1}^K |D_k|^2 \sum_{j=1}^K |S_j|^2 - \left| \sum_{k=1}^K D_k^* S_k \right|^2 \\
&= Q \sum_{k=1}^K |D_k|^2 - \left| \sum_{k=1}^K D_k^* S_k \right|^2 - \gamma \sum_{k=1}^K |D_k|^2.
\end{aligned}$$

To establish the equality of (12) and (13), add  $\gamma \sum_{k=1}^K |D_k|^2$  to both sides and divide by  $Q$ .

## APPENDIX B. DERIVATION OF GRADIENT FORMULAS

The Gateau derivative, or variation, of  $J$  in the direction  $\psi$  is given by

$$\delta_\psi J[\phi] = \lim_{\tau \rightarrow 0} \frac{J[\phi + \tau\psi] - J[\phi]}{\tau} = \frac{d}{d\tau} J[\phi + \tau\psi] \Big|_{\tau=0}.$$

The derivative  $J'[\phi]$  (which is the gradient of  $J$ ) is characterized by

$$\delta_\psi J[\phi] = \langle \psi, J'[\phi] \rangle$$

for any direction  $\psi$ . By the linearity of the operator  $\delta_\psi$ , (11)-(12), and (19),

$$\delta_\psi J[\phi] = -\frac{1}{2} \delta_\psi \int \int \frac{P[\phi] P^*[\phi]}{Q[\phi]} + \alpha \langle \psi, \mathcal{A}^{-1} \phi \rangle, \quad (29)$$

where

$$P[\phi] = \sum_k D_k^* S_k[\phi], \quad Q[\phi] = \gamma + \sum_k S_k[\phi] S_k^*[\phi]. \quad (30)$$

Now by the product and quotient rules for differentiation,

$$\begin{aligned}
\delta_\psi \int \int \frac{P[\phi] P^*[\phi]}{Q[\phi]} &= \int \int \frac{Q \delta_\psi (P[\phi] P^*[\phi]) - |P|^2 \sum_k \delta_\psi (S_k[\phi] S_k^*[\phi])}{Q^2} \\
&= \int \int \sum_k \delta_\psi S_k[\phi] \left( \frac{P^* Q D_k^* - |P|^2 S_k^*}{Q^2} \right) + c.c. \\
&= \sum_k \langle \delta_\psi S_k[\phi], V_k \rangle + c.c., \quad (31)
\end{aligned}$$

where “c.c.” denotes the complex conjugate of the previous term, and

$$V_k = \frac{P Q^* D_k - |P|^2 S_k}{Q^2} = F^* D_k - |F|^2 S_k.$$

The second equality follows from (30) and (9). We now suppress the subscripts  $k$  and make use of various properties of the derivative, as well as (23)-(24). We also make use of the fact that the Fourier transform preserves angles to obtain

$$\begin{aligned}
\langle \delta_\psi S[\phi], V \rangle + c.c. &= \delta_\psi \langle S[\phi], V \rangle + c.c. \quad (32) \\
&= \delta_\psi \langle s[\phi], v \rangle + c.c., \quad v = \mathcal{F}^{-1}(V) \\
&= \delta_\psi \langle h[\phi] h^*[\phi], v \rangle + c.c. \\
&= \delta_\psi \langle h[\phi], h[\phi] v \rangle + c.c.
\end{aligned}$$

$$\begin{aligned}
&= \langle \delta_\psi h[\phi], hv \rangle + \langle h, \delta_\psi h[\phi]v \rangle + c.c. \\
&= \langle \delta_\psi H[\phi], \mathcal{F}(hv) \rangle + \langle \mathcal{F}(hv^*), \delta_\psi H[\phi] \rangle + c.c. \\
&= \langle i\psi H, \mathcal{F}(hv) \rangle + \langle \mathcal{F}(hv^*), i\psi H \rangle + c.c.
\end{aligned} \tag{33}$$

$$\begin{aligned}
&= \langle \psi, i^* H^* \mathcal{F}(hv) + iH \mathcal{F}^*(hv^*) \rangle + c.c. \\
&= \langle \psi, 4\text{Imag}[H^* \mathcal{F}(h\text{Real}[\mathcal{F}^{-1}(V)])] \rangle.
\end{aligned} \tag{34}$$

In (33) we have used (23) to obtain  $\delta_\psi H = \psi H$ . Equating the left hand side of (32) with (34) and then applying (31) and (29), we obtain the derivative, or gradient, of  $J$ ,

$$J'[\phi] = -2 \sum_k \text{Imag}[H_k^* \mathcal{F}(h_k \text{Real}[\mathcal{F}^{-1}(V_k)])] + \alpha \mathcal{A}^{-1} \phi.$$

### APPENDIX C. DERIVATION OF HESSIAN APPROXIMATIONS

From (13) and (18), the first term in (11) can be written as

$$J_{data}[\phi] = \frac{1}{2} \sum_{j < k} \sum \|R_{jk}[\phi]\|^2 + \frac{\gamma}{2} \|D^{1/2}[\phi]\|^2, \tag{35}$$

where

$$R_{jk}[\phi] = \frac{D_k S_j[\phi] - D_j S_k[\phi]}{Q^{1/2}[\phi]}, \quad D[\phi] = \frac{\sum_{k=1}^K |D_k|^2}{Q[\phi]}, \tag{36}$$

and  $Q[\phi]$  is defined in (14). Perhaps the simplest positive definite Hessian approximations can be constructed by dropping the second term on the right hand side of (35), fixing the  $Q$  in the first term, and applying the Gauss-Newton idea. Proceeding in this manner, define

$$\tilde{R}_{jk}[\phi] = \tilde{D}_k S_j[\phi] - \tilde{D}_j S_k[\phi], \tag{37}$$

where

$$\tilde{D}_k = \frac{D_k}{Q^{1/2}}. \tag{38}$$

Note that  $Q$  is fixed, so the  $\tilde{D}_k$  are independent of  $\phi$ . Then the action of the resulting operator, which we denote by  $\tilde{H}$ , is given by

$$\langle \tilde{H}\xi, \psi \rangle = \sum_{j < k} \sum \langle U_{jk}, \tilde{R}'_{jk}[\phi]\psi \rangle \tag{39}$$

where now

$$U_{jk} = \tilde{R}'_{jk}[\phi]\xi = \tilde{D}_k S'_j[\phi]\xi - \tilde{D}_j S'_k[\phi]\xi. \tag{40}$$

We next derive an expression for  $S'_j[\phi]\xi$ , where  $\xi \in L^2(\mathbb{R}^2)$  is fixed. Drop the subscript  $j$ , and let  $W$  be arbitrary. Then proceeding as in Appendix B with  $\xi$  and  $W$  playing the role of  $\psi$  and  $V$ , respectively,

$$\begin{aligned}
\langle S'[\phi]\xi, W \rangle &= \delta_\xi \langle S[\phi], W \rangle \\
&= \langle i\xi H, \mathcal{F}(hw) \rangle + \langle \mathcal{F}(hw^*), i\xi H \rangle, \quad w = \mathcal{F}^{-1}(W) \\
&= \langle ih^* \mathcal{F}^{-1}(\xi H), w \rangle + \langle i^* h \mathcal{F}^*(\xi H), w \rangle \\
&= \langle -2 \text{Imag}[h^* \mathcal{F}^{-1}(\xi H)], w \rangle.
\end{aligned}$$

Taking Fourier transforms,

$$S'[\phi]\xi = -2\mathcal{F}(\text{Imag}[h^* \mathcal{F}^{-1}(\xi H)]). \tag{41}$$

Consequently,

$$U_{jk} = -2\tilde{D}_k \mathcal{F}(\text{Imag}[h_j^* \mathcal{F}^{-1}(\xi H_j)]) + 2\tilde{D}_j \mathcal{F}(\text{Imag}[h_k^* \mathcal{F}^{-1}(\xi H_k)]). \tag{42}$$

Examining the terms in (39) and applying computations similar to those above,

$$\begin{aligned}
\langle U_{jk}, \tilde{D}_k S'_j[\phi]\psi \rangle &= \langle \tilde{D}_k^* U_{jk}, S'_j[\phi]\psi \rangle \\
&= \delta_\psi \langle \tilde{D}_k^* U_{jk}, S_j[\phi] \rangle \\
&= \langle 2\text{Imag}[H_j^* \mathcal{F}(h_j w_k)], \psi \rangle,
\end{aligned} \tag{43}$$

provided

$$w_k = \mathcal{F}^{-1}(\tilde{D}_k^* U_{jk}) \tag{44}$$

is real-valued. An analogous expression is obtained when  $\tilde{D}_k, S'_j$  are replaced by  $\tilde{D}_j, S'_k$ . Then combining (39) with (43),

$$\tilde{H}[\phi]\xi = 2 \sum_{j < k} \text{Imag}[H_j^* \mathcal{F}(h_j w_k) - H_k^* \mathcal{F}(h_k w_j)]. \tag{45}$$

### ACKNOWLEDGMENTS

The work of Curtis R. Vogel was supported by NSF under grant DMS-9622119 and AFOSR/DEPSCoR under grant F49620-96-1-0456. Tony Chan was supported by NSF under grant DMS-9626755 and ONR under grant N00014-19-1-0277. Support for Robert Plemmons came from NSF under grant CCR-9623356 and from AFOSR under grant F49620-97-1-0139. The authors wish to thank Brent Ellerbroek of the U.S. Air Force Starfire Optical Range for providing data, encouragement, and helpful advice for this study.

### REFERENCES

1. R. A. Gonsalves, "Phase retrieval and diversity in adaptive optics," *Optical Engineering*, **21**, pp. 829-832, 1982.
2. R. G. Paxman, T. J. Schulz, and J. R. Fineup, "Joint estimation of object and aberrations by using phase diversity," *J. Optical Soc. Am.*, **9**, pp. 1072-1085, 1992.
3. J. E. Dennis, Jr., and R. B. Schnabel, *Numerical Methods for Unconstrained Optimization and Nonlinear Equations*, SIAM Classics in Applied Mathematics Series, **16**, 1996.
4. J. W. Goodman, *Introduction to Fourier Optics, 2<sup>nd</sup> Edition*, McGraw-Hill, 1996.
5. B.L. Ellerbroek, D. C. Johnston, J. H. Seldin, M. F. Reiley, R. G. Paxman, and B. E. Stribling, "Space-object identification using phase-diverse speckle," in *Mathematical Imaging, Proc. SPIE*, **3170-01**, 1997.
6. M. C. Roggemann and B. Welsh, *Imaging Through Turbulence*, CRC Press, 1996.
7. D. W. Tyler, M. C. Roggemann, T. J. Schultz, K. J. Schultz, J. H. Selden, W. C. van Kampen, D. G. Sheppard and B. E. Stribling, *Comparison of image estimation techniques using adaptive optics instrumentation, Proc. SPIE* **3353**, 1998 (these Proceedings).
8. B. L. Ellerbroek, B. J. Thelen, D. J. Lee, D. A. Carrara, and R. G. Paxman, *Comparison of Shack-Hartman wavefront sensing and phase-diverse phase retrieval*, Adaptive Optics and Applications, R. Tyson and R. Fugate, editors, *Proc. SPIE* **3126**, pp. 307-320, 1997.